communications materials

Article

https://doi.org/10.1038/s43246-024-00652-8

Direct quantitative assessment of single-atom metal sites supported on powder catalysts

Paula Aniceto-Ocaña, José Marqueses-Rodriguez, José A. Perez-Omil, José J. Calvino, Carmen E. Castillo & Miguel Lopez-Haro

Rational design of effective catalyst demands a profound understanding of active-site structures. Single-atom supported powder catalysts, depicting unique features like enhanced metal dispersion, hold promise in different applications. Here, we present an approach to directly quantify the detailed structural nature of metal sites in single-atom, high surface area, powder catalysts. By combining advanced high-resolution scanning-transmission electron microscopy, deep learning and density functional theory calculations, we determine, with statistical significance, the exact location and coordination environment of Pd single-atoms supported on MgO nanoplates. Our findings reveal a preferential interaction of Pd single-atoms with cationic vacancies (V-centers), followed by occupation of anionic defects on the {001} MgO surface. The former interaction results in stabilization of PdO species within V-centers, while partially embedded Pd states are found in F-defects. This methodology opens a route to the ultimate structural analysis of metal-support interaction effects, key in the design of advanced nanocatalysts for sustainable and energy-efficient processes.

The use of single atoms catalysts (SACs) has attracted a large attention because of their excellent properties, when compared to their nanoparticles counterpart, in terms of reactivity in many different reactions, particularly in the field of Environmental Catalysis and Clean Energy[1,2]. These species are supported either on non-porous structures, typically oxides or carbon-based materials, or hosted into crystalline porous materials, such as zeolites or metal-organic frameworks (MOFs). Nonetheless, the performance of these species are highly influenced by the local atomic environment, *i.e.* the specific interaction with the support, and the structural characteristics of these metal entities[3]. In particular, when a non-porous structured material is employed as support, the large heterogeneity of the surfaces exposed by the crystallites and the presence of surface defects provide a large variety of anchoring sites for the atomically-dispersed species, with differing electronic and geometric properties and, therefore, distinct catalytic performances.

The exact structural characteristics of these differing sites are mainly related to both metal-metal and metal-support interactions. Hence, tailoring these structural characteristics opens a route to modulate the reactivity of this type of catalysts. In this sense, great efforts have been paid not only in the development of synthetic methods to control as much as possible structural features but also in the development of characterization techniques enabling a discrimination of key aspects like atomicity, composition, geometry and local environment of the metal species[4,5].

Regarding characterization, high resolution high angle annular dark Field scanning transmission electron microscopy (HR HAADF-STEM) imaging has consolidated as the only tool to directly visualize single metal atoms in high surface area, powder type, catalysts. The unique characterization capabilities of HAADF-STEM rely on the two following questions: (i) it allows imaging matter with sub-Angstrom spatial resolution, (ii) the signal collected to build the image is proportional to roughly the squared atomic number Z^2. Therefore, it provides images with chemical contrast[6]. However, most studies reported in recent years exploiting HAADF-STEM images to detect single metal atoms or subnanometric metal clusters supported on non-porous or porous oxides, use this technique simply in a qualitative way[7]. In fact, only a few reports extract quantitative information about relevant structural features of SACs. Among these, we should mention the work of Chang et al., focused on the atomic-scale examination of the local coordination environments of isolated Pt atoms in various single-atom catalyst (SAC)[8]. In this case, a preferential anchoring of Pt atoms at vacancy sites neighboring basal oxygen atoms in subsurface positions was reported. While this study provided valuable insights, SACs were manually identified on the images, a strategy that does not only limit the size of the observation set but also introduces some degree of subjectivity when selecting each observation. Moreover, the sample preparation method used in this study, which involved vacuum evaporation of Pt, diverges significantly from the

Departamento de Ciencia de los Materiales e Ingeniería Metalúrgica y Química Inorgánica. Facultad de Ciencias, Campus Rio San Pedro S/N. Puerto Real, Cádiz, Spain. e-mail: miguel.lopezharo@uca.es

more prevalent wet impregnation technique routinely used to prepare metal-SACs supported on oxides.

In another contribution, De Rita et al. delved into the local coordination environments of isolated Pt atoms supported on anatase-TiO_2 using in-situ and ex-situ scanning transmission electron microscopy (STEM) as well as spectroscopic techniques. Their findings pointed out to a preferential Pt-Ti interaction, particularly evident under hydrogen environment[9].

More recently, Büchel *et al.* explored the metal local environment of Pt atoms on carbon nitrides, employing a comprehensive battery of techniques including HR-HAADF microscopy, density functional theory (DFT) calculations, X-ray photoelectron spectroscopy (XPS), and nuclear magnetic resonance (NMR). However, they recognized limitations to provide information about the local metal environment with statistical significance. As a result, they claim for the implementation of automated methods to extract this crucial data[5]. Regarding this suggestion, state-of-the-art algorithms, based on artificial intelligence (AI) methods, are opening new opportunities in the automated analysis of digital images. If properly applied to aberration-corrected (AC)-STEM experiments, tools based on this approach could provide additional and relevant knowledge about the structural characteristics and local atomic environment of complex materials. Actually, most current trends clearly point out that AI techniques will become an indispensable tool for the ultimate analysis of STEM data, particularly in the case of large datasets[6]. In materials with an intrinsic heterogeneity as large as that commonly present in powder-type supported catalysts, the analysis of large volume datasets becomes a must if significant conclusions about structure are sought.

Among AI techniques, those based on deep learning (DL) methods are getting an increasing relevance[10]. DL proceeds by analyzing a huge amount of data. To process these data, AI algorithms are trained using models with features similar to those present in the input data to be analyzed. This training step is crucial when we are dealing with single atoms catalysts and, in general, key to get a good performance of supervised DL algorithms. Although many different DL methods are available, convolutional neural networks (CNNs) are to date those showing the best performance and most widely used for processing digital images. In particular, CNNs methods have been very recently used to denoise, segment and identify features of interest in HAADF-STEM images[11].

In the particular case of SACs, Mitchell et al. used CNNs to statistically characterize Pt and Fe SACs supported on carbon nitride[12]. More recently, Ni et al. also employed a CNN architecture to quantify the spatial arrangement of various adatom configurations supported on a carbon substrate, specifically focusing on determining the atomicity of these species with statistical significance[13]. However, these studies do not evaluate the local coordination environment of the metal; a quite important feature, intimately connected to the actual nature of metal-support interactions. To reveal this key aspect, it is necessary to determine in quantitative terms subtler details of the metal site structure, a quite challenging task in single-atom supported powder catalysts.

Our work faces this challenge, focusing specifically on Pd SACs anchored onto a high surface area MgO support; a family of catalysts with promising potential applications in various reactions within the field of Catalysis, as reported in recent contributions. Thus, Sarma et al. have investigated the catalytic activity of Pd SACs supported on MgO for CO oxidation, attributing the catalytic performance to the presence of oxidized Pd species[14]. Another study, by Guo and co-workers[15], demonstrated that Pd SACs supported on MgO exhibited high performance in the semi-hydrogenation of acetylene to ethylene. More recently, Chen et al. studied the catalytic activity of Pd SACs supported on MgO for ethylene hydrogenation. They identified two distinct Pd species: Pd cations located at the MgO steps and Pd atoms embedded in the first subsurface layer of MgO, attributing the best catalytic activity to the species found at the steps. This work underscores the key influence of the exact location of Pd atoms on catalytic performance, highlighting the need for a more in-depth analysis of structural features and metal-support interactions[16].

As a major goal, our study aims at evaluating, with statistical significance and high accuracy, the exact location of the metal species in support crystallites with intricate texture. To this end, we explore the combined use of complementary CNN algorithms with DFT calculations for a reliable and fully quantitative assessment of the ultimate structural features of metal-support interactions in SACs prepared on powder type, high surface area, non-porous oxide supports. It should be also noticed that the results obtained by combining CNN algorithms with DFT calculations were complemented and matched with others coming from macroscopic techniques like XPS, to provide a more complete picture of the single atom-support interactions responsible of the final performance of these systems. The methodology here developed, amenable to many other supported metal systems, contributes to bridging the gap between theoretical predictions and experimental observations, thereby advancing the field of heterogeneous catalysis in terms of fundamental knowledge.

Results and discussion

Study of the crystallographic nature of the surface exposed by the support

Evaluating metal-support interactions in powdered catalysts requires knowledge about the crystallography of the surface exposed by the support crystallites, a task of considerable complexity. In this study a high surface area MgO support was chosen due to the possibility of eventually controlling the surface properties and, at the same time, facilitating a high dispersion of the metal atoms. Furthermore, the low atomic number of the constituting elements, $Z_{Mg} = 12$ and $Z_O = 8$, makes of MgO a good choice for observing and analyzing individual atoms at the atomic scale with HAADF-STEM.

The support was prepared transforming commercial MgO into $Mg(OH)_2$ via a hydrothermal method, followed by a post-treatment in H_2(5%)/He at 900 °C for 6 h to achieve the final plate-like morphology. The X-ray powder diffraction diagram (PXRD), Supplementary Fig. 1a, b, reveals the peaks of periclase, indicating a complete transformation of $Mg(OH)_2$ into the corresponding oxide. Refinement of the experimental PXRD data reveals that the support consists of MgO crystals approximately 25 nm in size. BET measurements provided a specific surface area of 80 m^2/g, Supplementary Fig. 2. A simple calculation considering the density of MgO indicates that an 80 m^2/g surface area requires 21 nm crystallites, a value quite close to that determined by PXRD

Textural features, encompassing external morphology and crystallographic planes exposed at the surface were analyzed using HAADF-STEM electron tomography (ET) and high-resolution transmission electron microscopy (HREM). Figure 1a displays the volume rendering of a representative reconstruction of a MgO nanocrystal. Note that the crystallites depict an overall hexagonal morphology and that they are built up by the assembly of a huge number of small, roughly 25 nm in size, nano-cubes, in good agreement with PXRD analysis. The result is a porous texture, as clearly observed in the orthoslices extracted from the reconstructed volume, Fig. 1b–d.

Figure 1e displays a representative aberration-corrected high-resolution electron microscopy (AC-HREM) image of a MgO hexagonal-shaped aggregate. The digital diffraction pattern (DDP), extracted from the marked area, reveals distances and angles consistent with the {200} planes in the <001> zone axis of MgO. Note that the MgO crystallite is made up, in good agreement with ET, by small cubes limited by stepped {001} facets. Importantly, these textural features agree perfectly with the mechanism proposed by Thomele et al.[17]. These authors reported that after annealing at 900 °C and exposure to O_2, MgO nanostructures derived from the transformation of $Mg(OH)_2$, fully convert into MgO(100) nanocubes due to the removal of the hydroxyl groups responsible for stabilizing the MgO (111) surfaces. Consequently, based on the results obtained from our analysis and considering the mechanism proposed, the crystallographic surface exposed by the MgO nanoplates is predominantly {001}.

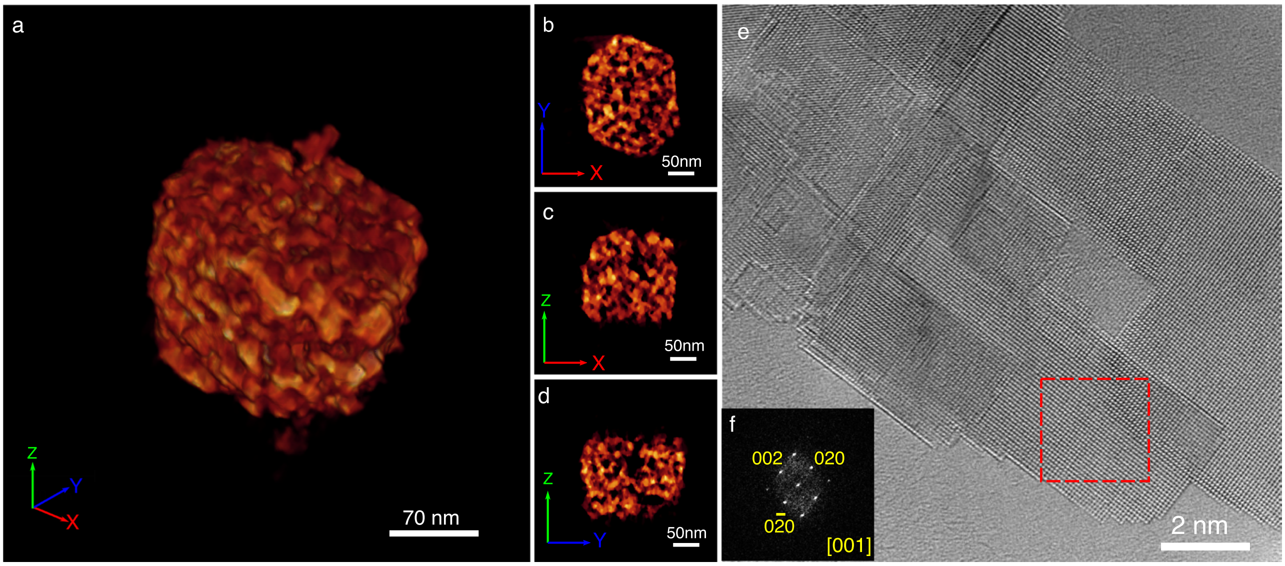

Fig. 1 | Textural and crystallographic study of MgO nanoplates. Volume rendering of the HAADF-STEM electron tomography reconstruction of MgO nanoplates **a**; slices cut through the reconstructed volume along the XY **b**, XZ **c** and YZ **d** planes; **e** Aberration-corrected HREM image of a MgO nanoplate; **f** Digital Diffraction Pattern obtained from the red-dashed square in (**c**).

Quantitative assessment of SACs-Support interactions

The Pd SACs were supported on the MgO {001} nanoplates by using wet chemical methods (see methods section) and further treated in O_2/He at 500 °C. PXRD (Supplementary Fig. 1 b) and BET technique (Supplementary Fig. 3) indicate that there is no significant modification of the support structure or texture after preparing the catalyst.

Figure 2 gathers representative HR-HAADF STEM images acquired on the Pd catalyst supported on MgO {001} nanoplates, recorded along four major MgO crystallographic orientations: <100 > , Fig. 2a, <110 > , Fig. 2b, <111 > , Fig. 2c and <211 > , Fig. 2d. Notably, all the images reveal the presence of bright spots with different intensity levels, as shown in the profiles extracted from images along the different orientations, Supplementary Fig. 4. Based on the contrast mechanism inherent to HAADF imaging, the more intense spots can be attributed to sites where individual Pd atoms locate ($Z_{Pd} = 46$), while the less bright ones should correspond to Pd-free, either pure Mg columns ($Z_{Mg} = 12$) or mixed Mg-O columns. Finally, the darker regions would locate on pure oxygen anionic columns ($Z_O = 8$). It is important to highlight that the very light O columns exhibit weak signals and cannot be effectively captured in HAADF mode.

To explore the influence of the starting metal precursor on the final structure, different catalysts were prepared. The differences observed in the number of individual species per surface unit between the different images is linked to this synthesis parameter. Specifically, images obtained along <100> (Fig. 2a), <110> (Fig. 2b), and <111> (Fig. 2c) come from a catalyst prepared from a Pd(II) complex, whereas the image recorded along <211> (Fig. 2d) was recorded on a sample in which $Pd(NO_3)_2$ was used as precursor. As commented in more detail below, no other influence of the metal precursor on the catalyst structure was observed.

For a more detailed examination of these species, specific regions were selected from each image in the complete set of HR-HAADF STEM results, as illustrated in Fig. 2e–h. Regardless of the precursor, the contrasts due to Pd SACs consistently locate, in all the images, on atomic columns containing Mg^{2+} cations rather than just O. Importantly, the applied imaging conditions did not lead to noticeable beam-induced alterations in the position of the atomic contrasts, as is shown in Supplementary Fig. 5. In fact, this result agrees with previous HR-HAADF studies performed on highly dispersed transition metals supported either on MgO (111) nanoplates[18] or MgO nanocrystals[14,19].

The expectation is that the location and arrangement of the metallic species is mainly influenced by their specific interactions with the support. These will depend on factors like the electronic state of the metallic atoms, the characteristics of the crystallographic surface and the presence of defects in the support, among others[3].

Turning our attention specifically onto the location of Pd species on the MgO nanoplates, just those images in both <110> and <211> zone axis (Fig. 2f and h), in which the atomic columns comprise only either Mg or O atoms, as illustrated in Supplementary Fig. 6c, d, offer the potential to distinguish the nature of the interaction at play, see Supporting information for further explanation.

In fact, in the experimental images recorded along both these orientations, Pd species locate on the atomic columns whose contrasts can be attributed to pure cationic columns. Importantly, simulated HR-HAADF images, Supplementary Fig. 7, confirm that Pd atoms could be visualized in both Mg and O positions even in the case of 36 nm thick crystals. Indeed, Supplementary Fig. 7d plots the variation of the intensity in different locations of the simulated images as a function of MgO crystal thickness, indicating that the detection of a Pd atom on a Mg column could be extended much further, since there is still a considerable difference between the intensities of the contrasts of these two types of columns in the case of the thickest, 36 nm, crystal.

On the other hand, it is important to mention that the HREM image in Fig. 1 clearly reveals steps on the {001} surfaces of the nanocubes. However, the HAADF-STEM images were recorded in planar view, in which Pd atoms are predominantly located in the central areas of the crystals. The question arises if the steps can be effectively and reliably detected under these particular imaging conditions. Therefore, to further investigate the presence of steps on the {001} surface, HR-HAADF STEM image simulations in the <211> orientation were conducted, as illustrated in Supplementary Fig. 8. Specifically, the simulated images of two different structural models were obtained and analyzed. In one of these models, a Pd atom was placed in a Mg vacancy on a completely flat surface (Supplementary Fig. 8a). In a second one, a step was added just on top of the Pd atom (Supplementary Fig. 8b). In addition, to ensure that the simulations closely resembled the experimental data, we considered the characteristics of the HAADF detector and incorporated the noise present in the experimental images into the simulated ones.

Notably, in the noise-free HAADF-STEM image simulations, the images exhibit quite similar contrasts, making it difficult to determine whether the Pd atoms are located or not at steps. As clearly shown in this figure, the comparison of the intensity profiles extracted from both

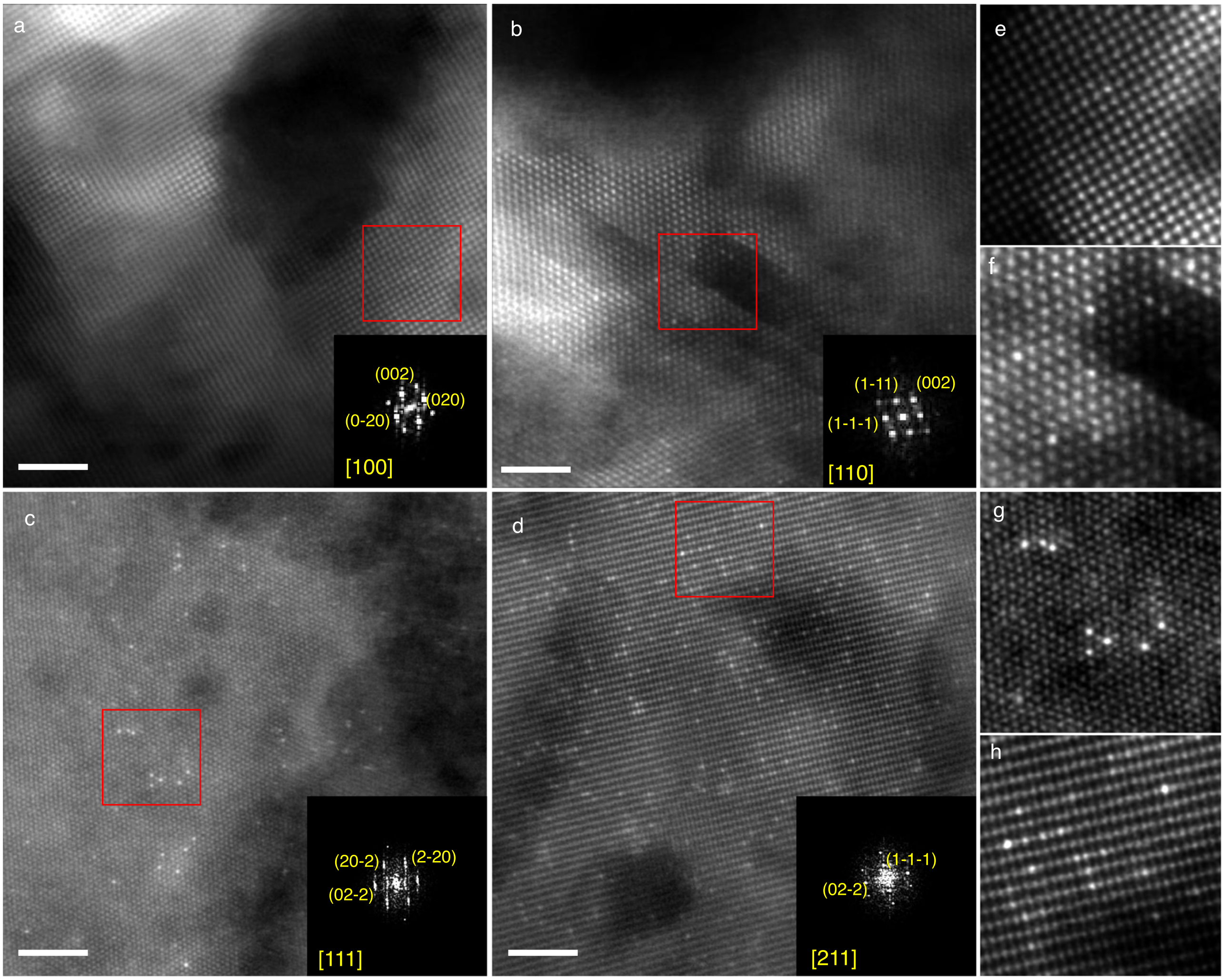

Fig. 2 | Experimental HR-HAADF STEM images of Pd/MgO {001} nanoplates in different orientations. < 100> **a**; <110> **b**; <111> **c** and <211> **d** zone axis. Insets show the corresponding DDPs. Specific regions extracted from the HAADF images for <100> **e**, <110> **f**, <111> **g** and <211> **h** orientations are also shown. Scale bar is 2 nm.

simulated images indicates only subtle intensity changes in the intensity of the Mg columns on the model sites where the step is present. In fact, in the presence of noise, these differences are completely wiped out, rendering the distinction between the two situations not viable, as indicated by the corresponding intensity profiles. Therefore, there will very likely be steps in the sample area imaged in Fig. 2 but, according to these simulations, it is not possible neither to detect where these locate nor if Pd is associated to this type of defect.

To improve the analysis of these observations and accurately quantify the nature of metal-support interaction, with statistical robustness, a smart segmentation procedure was developed to analyze the HR-HAADF images in <211> orientation. This segmentation approach involved partitioning the images into its distinct constituents: the background and the objects of interest, *i,e* the atomic columns containing Pd single atoms and those containing only Mg. As previously mentioned, DL tools, particularly those used in the domain of computer vision, have proven highly beneficial for this image processing task. In particular, semantic segmentation methodologies have been harnessed to generate segmentation maps which effectively translate pixel values into class labels.

Since convolutional neural networks employing the U-net architecture have demonstrated remarkable performance in this task[20–22], we tuned an U-net network to automatically discriminate the different intensities found in the experimental images by semantic segmentation. It is worth noting that this segmentation process was conducted under supervision, *i.e.* after training the neural network.

To obtain the synthetic input images for training, we combined atomistic models with fractal surfaces, which allowed us to mimic the contrast homogeneities commonly found in experimental images. Further information about the generation of synthetic models and training are gathered in supporting information. Representative synthetic models are shown in Supplementary Fig. 9.

The accuracy of our procedure was evaluated by metrics precision based on true positive (TP), false positive (FP) and false negative (FN) measurements, Supplementary Table 1, 2. This analysis has been carried out using synthetic images which were not used in our training step, and their ground truth. The values obtained fall in a range which guarantee that the single atoms are efficiently separated from the contrasts of the support.

Figure 3 illustrates the result obtained after applying the segmentation process in the HR-HAADF image in <211> orientation. Note how the algorithm discriminates the contrasts belonging to atomic columns where Pd species locate from those corresponding to just Mg columns. Noteworthy, a good separation is achieved even in areas of the images with large brightness variations. Moreover, similar results were obtained in HR-HAADF images acquired on the other zone axis orientations, Supplementary Fig. 10 and Supplementary Fig. 11.

To determine the actual nature of the interaction between Pd SACs and the underlying support it is necessary to locate the position of the Pd contrasts with respect to the MgO framework. To conduct such study with a significant level of statistical confidence, an image post-processing methodology was devised, sketched in Supplementary Fig. 12. This procedure

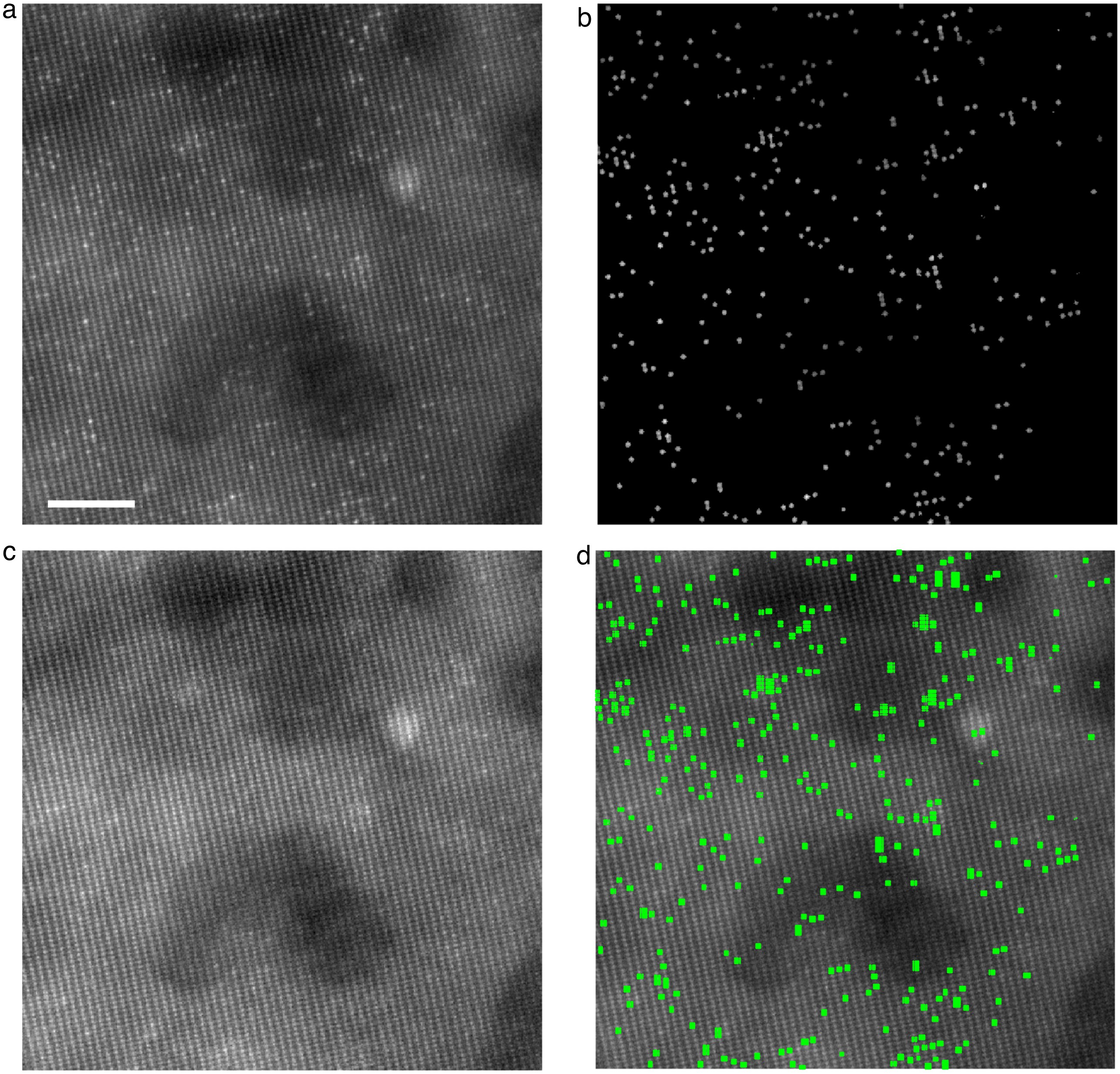

Fig. 3 | Deep learning segmentation and in-painting reconstruction. **a** Experimental HR HAADF-STEM image in <211> orientation. **b** Image segmentation of the Pd atoms using Deep Learning methods. **c** Reconstructed HR HAADF-STEM image of the MgO support in <211> zone axis by in-painting methods. **d** Image overlaying Pd pixels in contact with the support. The Pd-cationic column contacts are shown in green and in red those corresponding to Pd-anionic column contacts. The scale bar is 2 nm.

involves reconstructing an image of the bare support, Fig. 3c. Then, the degree of overlap between the pixels representing Pd SACs and those representing the support is assessed.

By processing a set of images in <211> zone axis using this procedure, close to 900 Pd-support interactions were evaluated. The outcome of this scrutiny unveiled that the entirety of Pd pixels exhibited immediate adjacency to the cationic columns, indicating a substantial interaction between the Pd species and Mg, as visually demonstrated in Fig. 3d, in which Pd atoms in contact with Mg columns are overlayed in green color. Of course, we are dealing with 2D images, which correspond to projections of a 3D structure, so these Pd species could be replacing some Mg or, instead, localized atop the cationic columns.

At this respect, it is important to mention that the investigated catalysts were submitted to a calcination process, which could have potentially resulted in positive oxidation state of the Pd species. Indeed, to evaluate the oxidation state of the catalyst XPS was conducted. Supplementary Fig. 13 to Supplementary Fig. 15 illustrates the spectrum obtained for Pd 3d, C 1 s and O 1 s respectively. It should be noticed how after deconvoluting Pd $3d_{5/2}$ and Pd $3d_{3/2}$ peaks, 336.1 and 341.1 eV is obtained. The values obtained can be assigned to Pd^{2+}, Supplementary Fig. 13. The oxidation state of these single atoms and the results obtained from the analysis of HR-HAADF STEM images, suggest that Pd species may be substituting Mg^{2+} ions, either on the surface or in subsurface positions of a {001} surface. The similarity of ionic radius of the two species (0.64 for Pd^{2+} and 0.65 for Mg^{2+}) could facilitate such substitution.

These results clearly contrast with those of Abbet et al. and, more recently, of Kropp et al., who have reported that Pd atoms stabilize on oxygen vacancies of MgO, known as F-centers. Nonetheless, it is important to note that these studies were carried out on model catalysts, which markedly differ from those prepared in this work via wet chemistry routes[23,24].

Our observations align with those of Sarma *et al.* who, in a study of Pd single atoms supported on powder type MgO, conclude that under oxidizing conditions, metal atoms exhibit a preference to substitute Mg atoms in the surface or subsurface layers, known in this case as V-centers[14]. A good agreement is also found with the combined EXAFS and HR-HAADF study of Ayin et al. showing that mononuclear osmium dicarbonyl species localize preferentially at Mg vacancies on MgO (110)[19].

In any case, figuring out the exact distribution of Pd, either in V or F sites or even both, becomes key to understand its actual electronic state and, of course, its catalytic performance. We have paid special attention to this particular question, which requires, as shown below, a more detailed analysis by both experimental and theoretical considerations.

DFT calculations of single Pd atom-support interactions

To unravel the mechanisms underlying Pd-support interactions, we conducted DFT calculations, carefully selecting assumptions and approximations that we believe are most closely aligned with the results obtained from the DL methodology. This approach was designed to ensure that the calculated results are as representative as possible of the actual system. While minor deviations from experimental observations may still occur due to the inherent limitations of DFT, we are confident that our model captures the key features of the Pd-support interactions.

These calculations assessed, in consecutive steps, three different questions: (i) the stability of surface defects on the MgO {100} surface, (ii) the interaction between Pd species and MgO {100} surfaces, and (iii) the relative position of single Pd species with respect to the surface. To accomplish this, 3×3 supercell models of a MgO {001} surface with one Pd species were built.

Starting with the first question, we examined Schottky, F-centers, and V-centers defect post-surface relaxation. Notably, Schottky defects entail ionized cation and anion vacancies in the stoichiometric ratio characteristic of the solid, while F and V centers are associated with neutral anion or cation vacancies, respectively. In the last two types of defects the lattice vacancy contains either two electrons (F center) or two holes (V center). These charge states could correspond to a modification of the oxidation state of the cationic/anionic species surrounding the vacancy. Specifically, the energy determination for Schottky defects yielded 4.49 eV. Defect formation energies on surfaces can vary significantly depending on the material and the type of defect. For MgO surfaces, Schottky defect formation energies are typically around 5 eV[25]. Our calculated value aligns well with those reported in the literature. This defect formation energy indicates that the expected concentration of Schottky defects on the MgO {001} surface will be very low. In any case, such concentration is expected to be much lower than those of V or F type centers, whose formation energy is lower.

In the case of F and V centers, it is important to mention that their presence is tied to the redox environment. For F-centers, energies of 6.67 eV and 3.71 were obtained under oxidizing and reducing conditions, respectively. This implies that, thermodynamically, at the surface, F-centers will only be significant under reducing conditions. Conversely, V-centers exhibited lower energy values for oxidizing conditions, 2.20 eV, compared to 5.16 eV for reducing ones.

According to these results, V-centers are expected to predominate under oxidizing conditions, while F-centers will be more prevalent under reducing environments, in good agreement with recent reports[26]. Therefore, one can reasonably anticipate that in our catalyst the V-type defects will be predominant given that the system underwent an oxidizing treatment. Nevertheless, a minor contribution of F defects cannot be completely ruled out. In fact, it is reported that both defects coexist at the surface of MgO in the temperature range in which the catalyst was treated[27,28].

In a second step, considering both the redox atmosphere and the experimentally observed oxidation state of Pd, we computed the interaction energy in three models; (i) Pd species inside {001} MgO F-centers, (ii) Pd species inside {001} MgO V-centers and (iii) PdO supported on a defect-free {001} MgO surface. The results obtained for an oxidizing atmosphere are gathered in Table 1.

Table 1 | DFT results of a model of Pd species on MgO {001} surface

Pd species within MgO {001} F-centers	Pd species within MgO {001} V-centers	PdO supported on defect-free {001} MgO surface
5.83 eV	0.24 eV	3.89 eV

Values of energy associated to the interaction of Pd single species with {001} MgO surface in oxidizing conditions.

Our calculations reveal that, under oxidizing conditions, Pd atoms will not tend to localize inside F-centers. However, despite the high energy value associated with this scenario, an interesting observation arises when considering the energy difference between Pd situated in an F-center and Pd positioned on a surface oxygen site. This difference yields a negative value of −2.71 eV, suggesting a preference for Pd to reside in the O_2^- vacancy rather than atop O_2. This preference is not solely due to the Pd atom itself, but it is also influenced by the apparent elimination or modification of the F-center. Essentially, if F-centers are present, there is a potential for metallic Pd to migrate towards them.

The energy values obtained from the other two models, 0.24 eV and 3.89 eV, indicate that the most stable configuration involves Pd inside V-centers. As previously mentioned, this center is neutral, creating two positive holes (h+) that are placed in two oxygen atoms around the vacancy. Consequently, a Pd inside a V-center is equivalent to PdO embedded in the MgO structure. This result suggests that the Pd single species in an oxidizing atmosphere show a preference for occupying the cationic defect rather than remaining supported.

Likewise, when assessing the energy difference between a Pd atom located on the surface and after incorporating into a V or F center, a much larger value is obtained for the former; −4.48 eV for the V center in comparison with −2.70 eV for the F-center. This suggests that in oxidizing conditions, Pd species first interact with V-centers, then likely occupy F-centers, and finally, reside atop the surface. Moreover, different authors suggest that those species are stabilized at the step[14,16]. Supplementary Fig. 16 displays the results obtained for Pd atoms localized in an atomic step. Note how the most stable situation is that in which Pd is occupied a V-center just adjacent to the step.

Note that this result aligns perfectly with our experimental observations, wherein the Pd species are localized within the Mg atomic columns. Furthermore, these calculations offer compelling evidence that Pd species are stabilized by occupying surface defects under oxidizing conditions, rather than remaining merely supported.

The analysis of the detailed structure of the relaxed models, in particular the relative height of Pd species within defects, has allowed us to gain crucial insights into Pd atom-support interactions. Thus, in the case of Pd species on MgO {001} F-centers, Pd tends to move slightly into the surface (when the starting position is above the surface, Fig. 4a) or outside the center (when the starting position is just embedded in the center, Fig. 4b), to finally position at an intermediate height over the vacancy, Fig. 4c. This results in a distance to the surface of 1.41 Å, a value significantly smaller than that expected for an atom just on the surface, 2.11 Å. Notably, this change in relative height is accompanied by a lateral displacement of 0.44 Å with respect to the position of the O column when projected along the <211> zone axis, as depicted in Fig. 4d. This visualization of the relaxed model highlights how Pd localizes between the O and Mg columns.

In the model of Pd embedded within V-centers, depicted in Fig. 4e, the displacement is much subtler, amounting to just 0.16 Å in the <211> projected structure, Fig. 4g. Along this direction, a slight deviation from the axis of the Mg column is observed. In contrast, Pd species positioned either on Mg or O columns show minimal displacements of 0.02 Å and 0.03 Å, respectively. In projection, these positions align seamlessly with the atomic columns.

Ultimate structural analysis at atomic scale. The differences observed in the lateral shifts of Pd could be potentially used to identify the type of

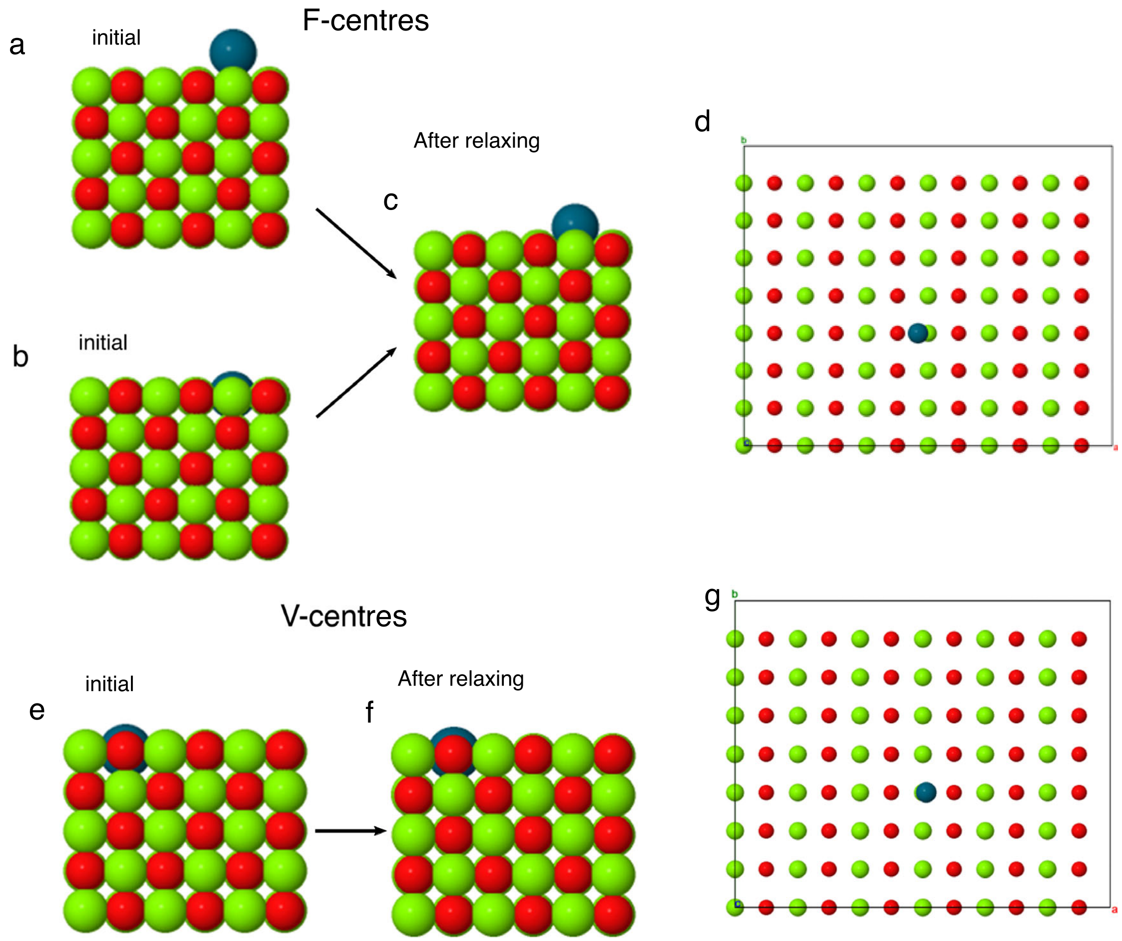

Fig. 4 | DFT computation of Pd single atom species on a MgO {001} surface. Unrelaxed model of a Pd atom on an F-center **a** and embedded in an F-center **b**. Relaxed model of a Pd atom on an F-center **c**. View of the relaxed model along the <211> zone axis **d**. Unrelaxed model of a Pd atom embedded in a V-center **e** and after relaxation **f**. Relaxed model of the Pd atom on a V-center along the <211> zone axis **g**.

site occupied by Pd from a precise analysis of HR-HAADF images recorded along the <211> zone axis. To evaluate this possibility, a HR-HAADF image simulation study was first conducted on structural models in which Pd is occupying both an F and V center, Supplementary Fig. 17. The image corresponding to the F-center clearly manifests an asymmetry in the contrasts of the Pd species (Supplementary Fig. 17a–c). When Pd is embedded in a V-center (Supplementary Fig. 17d–f), this feature is less pronounced but still present.

These asymmetries translate into subtle displacements in the center of mass of the atomic column contrasts in the experimental HR-HAADF images. However, to detect these displacements quite accurate measurements are required. Therefore, to provide the finest detail possible about the nature of metal support interactions, we developed a methodology to reliably perform these measurements. This methodology uses the pre-trained AtomSegNet routine[29].

This routine, based on a pre-trained deep learning technique capable of localizing, denoising, and implementing super-resolution techniques on experimental HR-HAADF STEM images, has demonstrated an exceptional performance in atom detection and localization under challenging contrast conditions, consistently surpassing the precision of state-of-the-art 2D Gaussian fit methods. Notably, the reported precision is 7.14 pm in the a-direction and 6.78 pm in the b-direction, showcasing sub-pixel accuracy. It is crucial to note that these values are much lower than the displacements expected for Pd species localized on both F and V centers (0.44 and 0.16 Å respectively).

The analysis of these displacements was conducted locally, using the segmented images of the Pd species and the reconstructed support images along the <211> zone axis. Our methodology began with a super-resolution task, followed by denoising, background removal, and ultimately extracting x-y coordinates for Pd atoms and Mg atomic columns with sub-pixel resolution. Supplementary Fig. 18 illustrates the workflow developed for this analysis.

The displacement of Pd atoms in the experimental images was calculated based on Euclidean distance, and both vector and modulus maps were estimated for each Pd species detected in the images. This process was applied to the entire set of cropped images.

Figure 5 illustrates the use of this method on the HAADF image in Fig. 3a. In particular, Fig. 5a shows different cropped regions, Fig. 5b the reconstructed support from these regions and Fig. 5c the segmented Pd atoms detected in these regions. Figures 5d,e map the displacement vectors and modulus of these vectors, respectively. Noteworthy, small displacements, falling in the 0.1 to 0.6 Å range could be measured.

The histogram of the displacement modulus after measuring a total of 900 Pd species, Fig. 6, spans the 0 to 0.9 Å range and reveals two major contributions. The first one, ranging from 0.11 to 0.3 Å, exhibits an asymmetrical peak centered around 0.2 Å. The second contribution, covering the 0.35 to 0.55 Å range, displays a maximum at roughly 0.4 Å. Values outside these ranges, below 0.11 Å or above 0.55 Å should be attributed to (i) species that experience no displacement and (ii) errors in the method. In any case, these represent at most 9% of the total number of measurements.

To extract quantitative information, the histogram was fitted by using a gaussian mixture model (GMM), a probabilistic framework that models data as a combination of multiple gaussian distribution. In particular, to find the optimum numbers of gaussian curves, we used the akaike information

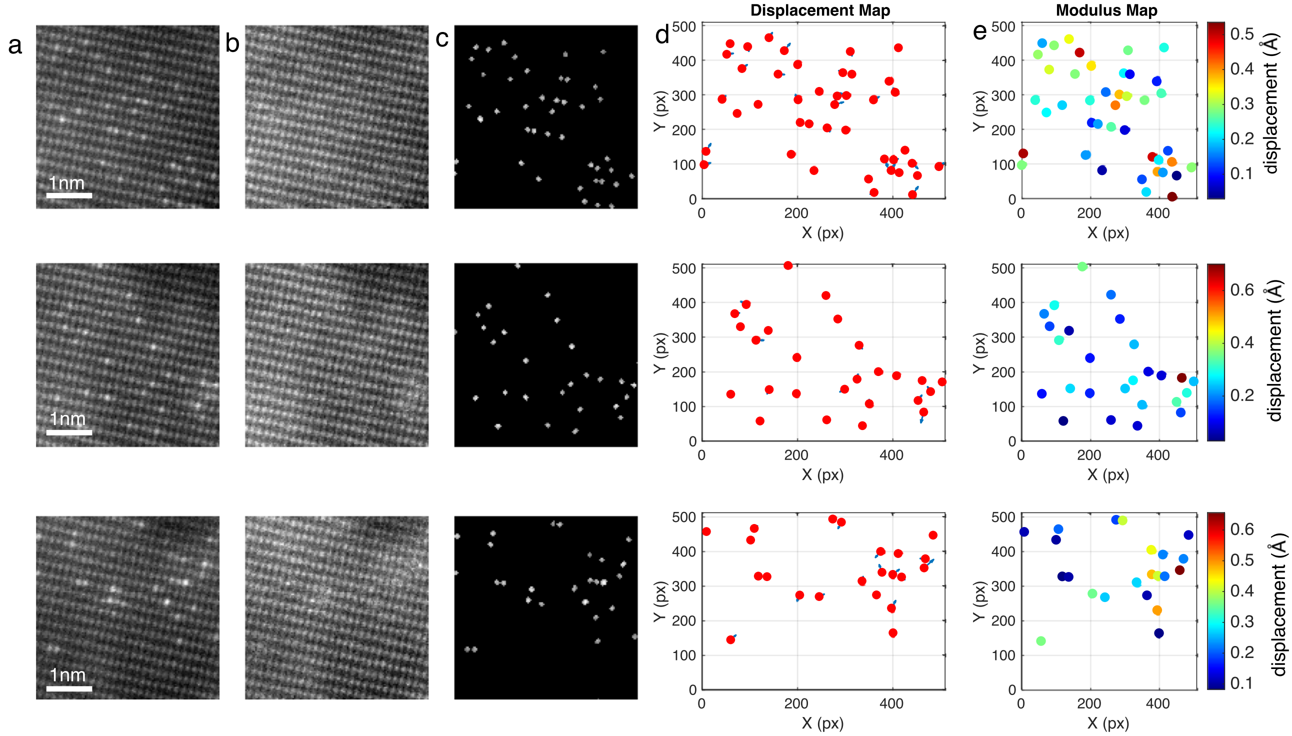

Fig. 5 | **Measurement of Pd atom displacements.** **a** Cropped images from the entire HAADF image; **b** reconstructed supports; **c** Pd atoms segmentations; **d** displacement maps and **e** modulus map **e**.

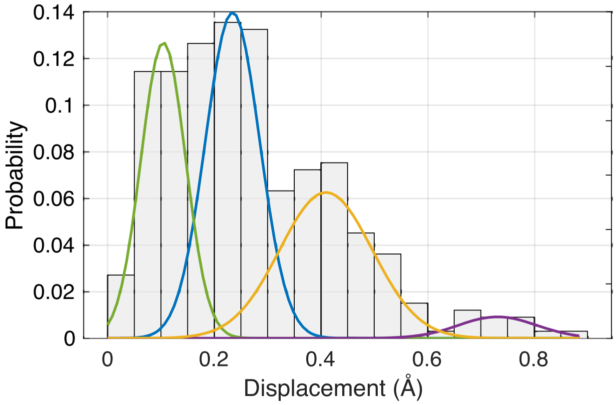

Fig. 6 | **Statistical analysis of measurement of Pd atom displacements.** Histogram of Pd species displacements. Fitting of the two major contributions are shown in yellow.

criterion (AIC). For our dataset, the AIC revealed a plateau with a minimum between four and five components, indicating that these options provided the optimal balance (Supplementary Fig. 19). We ultimately selected the model with four Gaussian components, as it offered the most appropriate trade-off for our analysis. The fitting indicates that the first peak (in green) is centered at 0.11 Å. This displacement could be related to either species that experience no displacement. The second peak (in blue) and the third peak (in yellow), centered at 0.22 Å and 0.41 Å respectively, aligning with the displacements predicted by DFT for atoms in V and F centers. The latter peak (in purple), cantered at 0.75 Å, is attributed to errors in the method. Additionally, the gaussian curve areas exhibit a 3:1 ratio, indicating a prevalence of atoms with smaller displacement.

These experimental findings correlate perfectly with DFT calculations. In fact, the observed preferential interaction of Pd with V-centers, followed by F-center occupancy, aligns well with our theoretical predictions. Moreover, considering the specific surface area of the MgO support, the metal loading, and the V-to-F ratio, it is possible to estimate that the distribution of the total number of Pd atoms would require a content of cationic vacancies of roughly 1%; a value in the order reported in literature for powder type MgO[30].

Conclusions

The close agreement observed between the values obtained from the analysis of experimental images and those predicted from computational methods strongly support the methodology here developed. Importantly, this methodology provides insights into the exact chemical nature of the interaction between single atom species and support in high-surface area powder catalysts, an aspect yet unexplored in previous works. Specifically, we have proved using direct imaging techniques that Pd species stabilize preferentially inside surface-located V-centers on the MgO support, instead of remaining embedded in F-defects. This represents a large step forward in the structural analysis of SACs.

Agreement between the outcomes of the analysis of the experimental images and the results of macroscopic techniques (like XPS) also underscores the robustness of our methodology and strengthens the value of the conclusions drawn from an analysis like the one developed here, based on a synergistic integration of advanced AC-STEM, AI analysis and computational approaches, to unravel the ultimate nature of metal-support interaction effects. This is a key question in catalysis research, particularly in catalysis by single atoms in which the actual nature of the support site in contact with the metal atoms can largely influence their chemical properties.

Applying the developed approach to a variety of catalytic materials, insights into general principles governing metal-support interactions could be gained, allowing for the identification of both common trends and unique features specific to each system. From this perspective, the methodology here developed represents a promising tool for the advancement of fundamental and applied catalysis research.

Methods

Sample preparation

The synthesis of morphology-controlled MgO nanoplates was carried out using a hydrothermal method followed by a thermal treatment. A stainless

Teflon-lined autoclave was filled with 5 g of commercial MgO (Sigma Aldrich, ACS 97%) and 200 mL of Milli-Q water. The autoclave was then sealed and heated at 160 °C for 24 h in an oven. Afterwards, the resulting $Mg(OH)_2$ nanoplates were centrifuged twice at 3500 rpm for 10 minutes to eliminate the water, then the product was dried in an oven at 80 °C overnight. Once $Mg(OH)_2$ nanoplates have been synthesized, it was heated at 900 °C for 6 h in a 60 mL/min H_2(5%)/Ar flow.

Pd-based catalysts were synthesized using two precursors of the metallic phase: (i) $Pd(NO_3)_2$ in acetone as solvent and (ii) an aqueous solution of the coordination complex $[H_3PdL]^{5+}$ (L = 3,6,9,17,20,23-hexaazatricyclo [23.3.1.111,15]triaconta-1(29),11(30),12,14,25(26),27-hexaene[31], which was formed in water by mixing $Pd(NO_3)_2$ with the macrocyclic ligand L in a 1:1 molar ratio, and subsequently fixing the pH at 6 to maximize its formation.

Both catalysts were prepared following a semi-wetness impregnation method where a slight excess over the pore volume of support was used. The nominal metal loading was 0.1 and 0.2 wt.% for the catalysts prepared with the metallic salt and the coordination complex respectively. For the former catalyst, the solution containing the metallic precursor was poured drop wise over the support and dried at 80 °C in an oven. The latter catalyst, after adding the solution with the precursor, was stirred for 2 h at room temperature and then dried by lyophilisation. In each case, 1.5 g of MgO were impregnated. After the drying step, the samples were treated at 500 °C for 1 h in a O_2(5%)/He flow to eliminate the nitrate.

Macroscopic characterization

Palladium loading was determined by ICP-AES. ICP measurement was carried out using an ICP-AES Iris Intrepid equipment of Thermal Elemental.

Specific surface area was determined on a Micromeritics ASAP2020. Before the analysis, the sample was degassed for 2 h at 200 °C. Adsorption and desorption of nitrogen measurements were performed at −196 °C. Measurement of specific surface area was performed by a multipoint approach on the basis of the BET (Brunauer–Emmet–Teller) theory and equation.

The samples were macroscopically characterized using different techniques. The crystalline structure was studied by X-ray diffraction employing a Bruker D8 Advanced A25 diffractometer equipped with a LYNXEYE detector and a Cu Kα radiation source. XRD data analysis has been performed in PowderCell software, comparing theorical periclase (AMCSD code: 0000501) and brucite (AMCSD code: 0014731) crystallographic information with the experimental data. Refinement was performed by fitting the peaks profile with pseudo-Voigt functions. Quality of the process was judged from the R-values (Rwp and Rexp). Regarding crystal size, the reported value was obtained from the slope of the corresponding (Williamson-Hall plot).

X-ray photoelectron spectroscopy analysis has been performed on a Kratos Axis Ultra DLD spectrometer, spectra were collected using a non-monochromatized Mg Kα (1253.6 eV) to avoid the overlapping of Mg Auger signal and Pd 3d peak. The binding energy (BE) scale was corrected with respect to the position of adventitious carbon (284.8 eV).

TEM/STEM characterization

Electron tomography (ET) experiments were performed using a Talos FX200 G2 microscope operated at 200 kV. A convergence angle of 9.0 mrad was selected and HAADF detector were used. In particular, a camera length of 125 mm was used, providing a collection angle range from 91 to198. Tilt series were recorded using a Fishione 2020 holder from −70 to 70 each 5°.

The whole set of images was aligned by combining the cross-correlation method, using FEI Inspect3Dv4.1, and the landmark-based alignment implemented in TomoJ v2.31. Afterward, they were reconstructed into a 3D volume using a compressed sensing algorithm based on the minimization of the total variation(TVM). In particular, a 3D implementation of the TVAL3 routine, using an ASTAR toolbox, was employed. For visualization the reconstructed volume, the FEI Avizo Software were used.

Transmission and Scanning Transmission Electron Microscopy measurements were carried out on a FEI Titan[3] Themis 60-300 double aberration-corrected operated at 200 kV. For HREM images, the defocus and the third-order aberration coefficients of the objective lens were measured and adequately compensated for using the Zemlin tableau. The acquisition time was 1 s per image. The magnification used for recording the 2048 × 2048 digital images was in the range of 600 K − 1 M. The Diffraction Digital Patterns (DDPs) correspond to a log-scaled version of the modulus of the FFT of the square shaped regions of interest (ROIs) selected on the atomically resolved images. In order to improve the contrast and avoid the appearance of streaked spots, prior to FFT the chosen ROIs were cut using a soft-edge circular mask with total radius half that of the square size.

In the case of HR-HAADF images, the aberrations of the condenser lens were corrected up to fourth order using the Zemlin tableau to obtain a sub-Angstrom electron probe. A condenser aperture of 50 μm, resulting in a convergence angle of 19 mrad, was utilized. The annular dark-field (ADF) collection angle ranged from 48 to 198 mrad. Images with a size of 2048 × 2048 pixels were recorded with a beam current of approximately 30 pA and a dwell time of 1.25 μs.

HAADF-STEM image simulations

Structural models for HR-HAADF image simulation studies were constructed using RHODIUS[32], a computer program developed at Cadiz University. HR-HAADF images were calculated from these models using TEMSIM software[33]. The following optoelectronic parameters; $\Delta f = 3$ nm, acceleration voltage = 200 kV, $Cs_3 = -0.001$ mm, $Cs_5 = 5$ mm, $\alpha = 18$ mrad were employed. Analysis of HR-HAADF STEM images was performed using custom Matlab routines.

Deep learning Implementation

Deep learning algorithms were implemented in Tensor Flow and Keras in an Intel Core i9 − 10900 CPU@2.80 GHz with a GPU Nvidia GeForceRTX 3090. In particular, for segmentation a residual U-net structure using an AttenResUnet model was implemented. To train this model, 100 epochs were used with a batch size of 10, an Adam optimizer with a learning rate of 0.001, and a Binary Focal Loss was used as the loss function to avoid the disparity of classes.

DFT calculations

The DFT calculations were performed using the plane-wave code Quantum Espresso[34] with the spin polarized Perdew-Burke-Ernzerhof functional revised for solids (PBEsol)[35]. The appropriate Projected Augmented Wave (PAW) scalar relativistic pseudopotentials were used for the elements Pd, Mg and O[36]. A Hubbard U parameter for Pd is used (U = 5.0 eV) calculated through the density-functional perturbation theory available in the HP code[37]. An energy cutoff of 70 Ry was considered. The calculations were performed with a 8 × 8 × 8 Monkhorst–Pack grid or using the gamma point for unit cells or supercells, respectively. For the relaxation processes the Broyden–Fletcher–Goldfarb–Shanno (BFGS) algorithm for geometry optimization has been used.

Data availability

The experimental data that support the findings of this study are available from the corresponding author upon request.

Code availability

The code and scripts used in this work are available from the corresponding author upon request.

Received: 1 April 2024; Accepted: 23 September 2024;

References

1. Ding, S. P., Hülsey, M. J., Pérez-Ramírez, J. & Yang, N. Transforming energy with single-atom catalysts. *Joule* **3**, 2897–2929 (2019).

2. Beniya, A. et al. CO oxidation activity of non-reducible oxide-supported mass-selected few-atom Pt single-clusters. *Nat. Commun.* **11**, 1888 (2020).
3. Mitchell, S. & Pérez-Ramírez, J. Atomically precise control in the design of low-nuclearity supported metal catalysts. *Nat. Rev. Mater.* **6**, 969–985 (2021).
4. Liu, L. C. & Corma, A. Confining isolated atoms and clusters in crystalline porous materials for catalysis. *Nat. Rev. Mater.* **6**, 244–263 (2021).
5. Büchele, S. et al. Elucidation of metal local environments in single-atom catalysts based on carbon nitrides. *Small* **18**, 2202080 (2022).
6. Kalinin, S. V. et al. Machine learning in scanning transmission electron microscopy. *Nat. Rev. Methods Prim.* **2**, 11 (2022).
7. Liu, L. C. & Corma, A. Metal catalysts for heterogeneous catalysis: from single atoms to nanoclusters and nanoparticles. *Chem. Rev.* **118**, 4981–5079 (2018).
8. Chang, T. Y. et al. Direct Imaging of Pt single atoms adsorbed on TiO_2 (110) surfaces. *Nano Lett.* **14**, 134–138 (2014).
9. DeRita, L. et al. Structural evolution of atomically dispersed Pt catalysts dictates reactivity. *Nat. Mater.* **18**, 746–751 (2019).
10. Chen, K. & Barnard, A. S. Advancing electron microscopy using deep learning. *J. Phys. Mater.* **7**, 022001 (2024).
11. Botifoll, M., Pinto-Huguet, I. & Arbiol, J. Machine learning in electron microscopy for advanced nanocharacterization: current developments, available tools and future outlook. *Nanoscale Horiz.* **7**, 1427–1477 (2022).
12. Mitchell, S. et al. Automated image analysis for single-atom detection in catalytic materials by transmission electron microscopy. *J. Am. Chem. Soc.* **144**, 8018–8029 (2022).
13. Ni, H. Y. et al. Quantifying atomically dispersed catalysts using deep learning assisted microscopy. *Nano Lett.* **23**, 7442–7448 (2023).
14. Sarma, B. B. et al. Metal-specific reactivity in single-atom catalysts: CO oxidation on 4d and 5d transition metals atomically dispersed on MgO. *J. Am. Chem. Soc.* **142**, 14890–14902 (2020).
15. Guo, Y. L. et al. High performance of single-atom catalyst Pd_1/MgO for semi-hydrogenation of acetylene to ethylene in excess ethylene. *ChemNanoMat* **7**, 526–529 (2021).
16. Chen, Y. Z. et al. Dynamic structural evolution of MgO-supported palladium catalysts: from metal to metal oxide nanoparticles to surface then subsurface atomically dispersed cations. *Chem. Sci.* **15**, 6454–6464 (2024).
17. Thomele, D. et al. Cubes to cubes: organization of MgO particles into one-dimensional and two-dimensional nanostructures. *Cryst. Growth Des.* **21**, 4674–4682 (2021).
18. Fang, H. H. et al. Dispersed surface Ru ensembles on MgO(111) for catalytic ammonia decomposition. *Nat. Commun.* **14**, 647 (2023).
19. Aydin, C., Kulkarni, A., Chi, M. F., Browning, N. D. & Gates, B. C. Atomically resolved site-isolated catalyst on MgO: mononuclear osmium dicarbonyls formed from $Os_3(CO)_{12}$. *J. Phys. Chem. Lett.* **3**, 1865–1871 (2012).
20. Yang, S. H. et al. Deep learning morphological distribution analysis of metal alloy catalysts in proton exchange membrane fuel cells. *Mater. Today Energy* **36**, 101348 (2023).
21. Faraz, K., Grenier, T., Ducottet, C. & Epicier, T. Deep learning detection of nanoparticles and multiple object tracking of their dynamic evolution during in situ ETEM studies. *Sci. Rep.* **12**, 2484 (2022).
22. Horwath, J. P., Zakharov, D. N., Mégret, R. & Stach, E. A. Understanding important features of deep learning models for segmentation of high-resolution transmission electron microscopy images. *npj Comput. Mater.* **6**, 108 (2020).
23. Abbet, S., Heiz, U., Häkkinen, H. & Landman, U. CO oxidation on a single Pd atom supported on magnesia. *Phys. Rev. Lett.* **86**, 5950–5953 (2001).
24. Kropp, T., Lu, Z. L., Li, Z., Chin, Y. H. C. & Mavrikakis, M. Anionic single-atom catalysts for CO oxidation: support-independent activity at low temperatures. *ACS Catal.* **9**, 1595–1604 (2019).
25. van Gog, H. & van Huis, M. A. Structural and electronic properties of frenkel and schottky defects at the MgO{100} surface: spin polarization, mid-band gap states, and charge trapping at vacancy sites. *J. Phys. Chem. C.* **123**, 14408–14420 (2019).
26. Liu, P. et al. First-principle study on electronic structure and magnetism in doped MgO materials. *J. Supercond. Nov. Magn.* **35**, 2037–2045 (2022).
27. Murphy, D. & Giamello, E. A family of trapped electron centers on alkali-metal vapor doped magnesium-oxide. *J. Phys. Chem.* **99**, 15172–15180 (1995).
28. Wang, J. A. et al. Structural defects and acidic and basic sites in sol-gel MgO. *J. Phys. Chem. B* **101**, 7448–7451 (1997).
29. Lin, R. Q., Zhang, R., Wang, C. Y., Yang, X. Q. & Xin, H. L. L. TEMImageNet training library and AtomSegNet deep-learning models for high-precision atom segmentation, localization, denoising, and deblurring of atomic-resolution images. *Sci. Rep.* **11**, 5386 (2021).
30. Richter, N. A. *Charged point defects in oxides: a case study of mgo bulk and surface f centers*, TU Berlin, (2014).
31. Menif, R., Martell, A. E., Squattrito, P. J. & Clearfield, A. New hexaaza macrocyclic binucleating ligands-oxygen insertion with a dicooper(I) schiff-base macrocyclic complex. *Inorg. Chem.* **29**, 4723–4729 (1990).
32. Bernal, S. et al. The interpretation of HREM images of supported metal catalysts using image simulation: profile view images. *Ultramicroscopy* **72**, 135–164 (1998).
33. Kirkland, E. J. *Advanced Computing in Electron Microscopy*. (Springer 2010).
34. Giannozzi, P. et al. QUANTUM ESPRESSO: a modular and open-source software project for quantum simulations of materials. *J. Phys.: Condens. Matter* **21**, 395502 (2009).
35. Ropo, M., Kokko, K. & Vitos, L. Assessing the Perdew-Burke-Ernzerhof exchange-correlation density functional revised for metallic bulk and surface systems. *Phys. Rev. B* **77**, 195445 (2008).
36. Dal Corso, A. Pseudopotentials periodic table: From H to Pu. *Comput Mater. Sci.* **95**, 337–350 (2014).
37. Timrov, I., Marzari, N. & Cococcioni, M. HP - a code for the calculation of Hubbard parameters using density-functional perturbation theory. *Comput. Mater. Sci.* **279**, 108455 (2022).

Acknowledgements

This work has received support from Projects: PID2019-110018GA-I00 funded by MICIU/AEI/10.13030/501100011033, PID2020-113006-RB-I00 and PID2022-142312NB-I00 funded by MCIN/AEI/10.13039/501100011033 and by “ERDF A way of making Europe”. Project TED2021-130191B-C44 funded by MCIN/AEI/ 10.13039/501100011033 and European Union NextGenerationEU/PRTR) is also acknowledged. STEM experiments were recorded at the DME-UCA Node of the Spanish Singular Infrastructure for Electron Microscopy of Materials (ICTS ELECMI). P.A.O thanks FPI scholarship program from University of Cadiz.

Author contributions

M. L.-H. and C.E C. conceived the project and supervised the study. M.L.-H. and J.J.C. wrote the manuscript. P.A-O carried out the synthesis, structural characterizations with the collaboration of C.E.C. and contributed to the preparation of the manuscript. M.L.-H and P.A.-O carried out the high resolution STEM images. J.A.P.-O carried out the DFT calculations. J.M.-R. implemented the Deep Learning methods. All the authors discussed the results and contributed to the formation of the manuscript.

Competing interests

The authors declare no competing interests.

Additional information

Supplementary information The online version contains supplementary material available at https://doi.org/10.1038/s43246-024-00652-8.

Correspondence and requests for materials should be addressed to Miguel Lopez-Haro.

Peer review information *Communications Materials* thanks the anonymous reviewers for their contribution to the peer review of this work. Primary Handling Editors: Jet-Sing Lee

Reprints and permissions information is available at http://www.nature.com/reprints

Publisher's note Springer Nature remains neutral with regard to jurisdictional claims in published maps and institutional affiliations.

Open Access This article is licensed under a Creative Commons Attribution-NonCommercial-NoDerivatives 4.0 International License, which permits any non-commercial use, sharing, distribution and reproduction in any medium or format, as long as you give appropriate credit to the original author(s) and the source, provide a link to the Creative Commons licence, and indicate if you modified the licensed material. You do not have permission under this licence to share adapted material derived from this article or parts of it. The images or other third party material in this article are included in the article's Creative Commons licence, unless indicated otherwise in a credit line to the material. If material is not included in the article's Creative Commons licence and your intended use is not permitted by statutory regulation or exceeds the permitted use, you will need to obtain permission directly from the copyright holder. To view a copy of this licence, visit http://creativecommons.org/licenses/by-nc-nd/4.0/.

© The Author(s) 2024